Monthly Notices
of the
ROYAL ASTRONOMICAL SOCIETY

MNRAS **486,** 1781–1795 (2019) doi:10.1093/mnras/stz941
Advance Access publication 2019 April 4

Temporal correlation between the optical and γ-ray flux variations in the blazar 3C 454.3

Bhoomika Rajput,[1]★ C. S. Stalin,[1]★ S. Sahayanathan,[2] Suvendu Rakshit[3,4] and Amit Kumar Mandal[1,5]

[1] *Indian Institute of Astrophysics, Block II, Koramangala, Bangalore 560034, India*
[2] *Astrophysical Sciences Division, Bhabha Atomic Research Centre, Mumbai 400085, India*
[3] *Finnish Centre for Astronomy with ESO (FINCA), University of Turku, Quantum, Vesilinnantie 5, FI-20014 Turku, Finland*
[4] *Astrophysical Sciences Division, Bhabha Atomic Research Centre, Mumbai 400085, India*
[5] *Department of Physics, CHRIST (Deemed to be University), Hosur Road, Bangalore 560029, India*

Accepted 2019 March 28. Received 2019 March 28; in original form 2018 October 12

ABSTRACT

Blazars show optical and γ-ray flux variations that are generally correlated, although there are exceptions. Here we present anomalous behaviour seen in the blazar 3C 454.3 based on an analysis of quasi-simultaneous data at optical, ultraviolet, X-ray, and γ-ray energies, spanning about 9 yr from 2008 August to 2017 February. We have identified four time intervals (epochs), A, B, D, and E, when the source showed large-amplitude optical flares. In epochs A and B the optical and γ-ray flares are correlated, while in D and E corresponding flares in γ-rays are weak or absent. In epoch B the degree of optical polarization strongly correlates with changes in optical flux during a short-duration optical flare superimposed on one of long duration. In epoch E the optical flux and degree of polarization are anticorrelated during both the rising and declining phases of the optical flare. We carried out broad-band spectral energy distribution (SED) modelling of the source for the flaring epochs A,B, D, and E, and a quiescent epoch, C. Our SED modelling indicates that optical flares with absent or weak corresponding γ-ray flares in epochs D and E could arise from changes in a combination of parameters, such as the bulk Lorentz factor, magnetic field, and electron energy density, or be due to changes in the location of the γ-ray-emitting regions.

Key words: galaxies: active – galaxies: jets – galaxies: nuclei – quasars: individual: 3C 454.3 – gamma-rays: galaxies – X-rays: galaxies.

1 INTRODUCTION

Blazars are a peculiar class of active galactic nuclei (AGNs) that have their relativistic jets pointed close to the line of sight to the observer with angle $\leq 10^{\circ}$ (Antonucci 1993; Urry & Padovani 1995). They are classified as flat-spectrum radio quasars (FSRQs) and BL Lacerate (BL Lac) objects based on the strength of the emission lines in their optical/infrared (IR) spectrum. Both classes of objects emit radiation over the entire accessible electromagnetic spectrum from low-energy radio to high-energy γ-rays. As blazars are aligned close to the observer, the emission is highly Doppler boosted, causing them to appear as bright sources in the extragalactic sky. They dominate the extragalactic γ-ray sky first hinted by the Energetic Gammma-ray Experiment Telescope (EGRET) observations onboard the *Compton Gamma-Ray Observatory* (*CGRO*; Hartman et al. 1999) and now made apparent by the Large Area Telescope (LAT) onboard the *Fermi* Gamma-ray Space Telescope (Atwood et al. 2009). The broad-band spectra of blazars are dominated by emission from the jet with weak or absent emission lines from the broad-line region (BLR). One of the defining characteristics of blazars is that they show flux variations (Wagner & Witzel 1995) over a wide range of wavelengths on time-scales ranging from months to days and minutes. In addition to flux variations they also show large optical and radio polarization as well as optical polarization variability. In the radio band they have flat spectra with the radio spectral index (α_r) < 0.5 ($S_\nu \propto \nu^{-\alpha_r}$). The broad-band spectral energy distribution (SED) of blazars is characterized by a two-hump structure, one peaking at low energies in the optical/IR/X-ray region and the other one peaking at high energies in the X-ray/MeV region (Fossati et al. 1998; Mao et al. 2016). In the one-zone leptonic emission models, the low-energy hump is due to synchrotron emission processes and the high-energy hump is due to inverse Compton (IC) emission processes (Abdo et al. 2010b). The seed photons for the IC process can be either internal to the jet (synchrotron self-Compton or SSC; Konigl 1981;

★ E-mail: bhoomika@iiap.res.in (BR); stalin@iiap.res.in (CSS)

Marscher & Gear 1985; Ghisellini & Maraschi 1989) or external to the jet (external Compton or EC; Begelman et al. 1987). In the case of EC, the seed photons can be from the disc (Dermer & Schlickeiser 1993; Boettcher, Mause & Schlickeiser 1997), the BLR (Sikora, Begelman & Rees 1994; Ghisellini & Madau 1996), and the torus (Błaerrorzdotejowski et al. 2000; Ghisellini & Tavecchio 2008). Though leptonic models are found to fit the observed SED of a majority of blazars, for some blazars, their SEDs are also well fitted by either hadronic (Mücke et al. 2003; Böttcher et al. 2013) or lepto-hadronic models (Diltz & Böttcher 2016; Paliya et al. 2016). In the hadronic scenario, the γ-ray emission is due to synchrotron radiation from extremely relativisitic protons (Mücke et al. 2003) or the cascade process resulting from proton–proton or proton–photon interactions (Mannheim 1993). Even during different brightness/flaring states of a source, a single emission model is not able to fit the broad-band SED at all times. For example in the source 3C 279, while the flare during 2014 March–April is well fitted by a leptonic model (Paliya, Sahayanathan & Stalin 2015b), the flare in 2013 December with a hard γ-ray spectrum is well described by lepto-hadronic processes (Paliya et al. 2016). Thus, the recent availability of multiwavelength data coupled with studies of sources at different active states indicates that we still do not have a clear understanding of the physical processes happening close to the central regions of blazars.

An alternative to the SED-modelling approach to constrain the emission models in blazars is through multiband flux-monitoring observations. In the leptonic scenario of emission from the jets of blazars (Böttcher 2007), a close correlation between the optical and γ-ray flux variations is expected. However, in the hadronic scenario of emission from blazars (Mücke & Protheroe 2001), optical and γ-ray flux variations may not be correlated. Thus, optical and γ-ray flux variability observations could constrain the leptonic versus hadronic emission model of blazar jets. Recent observations made with the *Fermi* Gamma-ray Space Telescope (Atwood et al. 2009) coupled with observations in the optical and infrared wavelengths indicate that in the majority of blazars studied for flux variations, γ-ray flares are closely associated with flares detected at the optical wavelengths with or without lag (Bonning et al. 2009; Chatterjee et al. 2012; Liao et al. 2014; Carnerero et al. 2015). However, the availability of good time resolution of optical and γ-ray light curves has led to the identification of isolated flaring events in optical and γ-rays termed as 'orphan' flares. Both orphan γ-ray flares (prominent flare in GeV-band γ-rays with no corresponding flare in the optical band) and orphan optical flares (flaring event in the optical band with no counterpart in the γ-ray band) are now known in blazars. As of today, optical flares with no corresponding γ-ray flares are known in PKS 0208−5122 (Chatterjee et al. 2013a) and S4 1849+67 (Cohen et al. 2014) and γ-ray flares with no corresponding optical flares are known in PKS 2142−75 (Dutka et al. 2013), PKS 1510−089 (MacDonald et al. 2015), PKS 0454−234 (Cohen et al. 2014), and 3C 454.3 (Vercellone et al. 2011). We are carrying out a systematic analysis of the multiwavelength variability characteristics of a sample of blazars to (i) identify anomalous flux variability behaviour in blazars and (ii) constrain the physical processes happening in the central regions of blazars using flux variability and broad-band SED modelling. Here, we present our results on the brightest source in our sample 3C 454.3.

3C 454.3 is an FSRQ at a redshift $z = 0.859$. It was detected first as a bright and variable γ-ray source by EGRET onboard *CGRO* (Hartman et al. 1993). It has been studied extensively utilizing data over a large range of wavelengths that include optical, X-ray, and γ-ray energies (Bonning et al. 2009, 2012; Ackermann et al. 2010; Kushwaha et al. 2017). 3C 454.3 was found in a highly active state in the γ-ray band by AGILE (Vercellone et al. 2009, 2010) in 2007. In 2010 November the highest flare was detected at $E >$ 100 MeV with the LAT instrument, having a flux value of about 6.6×10^{-5} ph cm^{-2} s^{-1}(Abdo et al. 2011). According to Shah et al. (2017) X-ray and γ-ray emission from 3C 454.3 cannot be explained by a single emission mechanism and to study the high-energy observations one needs to consider both EC and SSC emission processes. We present here our results on the multiwavelength analysis carried out on the blazar 3C 454.3 using data that spans about 9 yr from 2008 August to 2017 February with the prime motivation to find a possible correlation between optical and γ-ray flux variations and subsequently constrain the emission processes in its central region. In Section 2, we present the data used in this work. The analyses are described in Section 3, followed by the results and discussion in Section 4. The results are summarized in Section 5.

2 MULTIWAVELENGTH DATA AND REDUCTION

We used all the publicly available multiwavelength flux monitoring data in γ-rays, X-rays, optical, UV, and IR bands that span about 9 yr covering the period 2008 August to 2017 February. We also used optical polarimetric data that were available for the above period.

2.1 γ-ray data

For γ-rays, we used the data from the LAT instrument onboard *Fermi*. The *Fermi*-LAT is a pair-conversion telescope sensitive to γ-ray energies from 20 MeV to more than 300 GeV (Atwood et al. 2009). *Fermi* normally operates in scanning mode and covers the entire sky once every ∼3 h. We used all the data for 3C 454.3 collected for the period 2008 August to 2017 February (MJD: 54500–57800; ∼110 months) and analysed using the Fermi Science Tool version v10r0p5 with appropriate selections and cuts recommended for the scientific analysis of PASS8 data.[1] The photon-like events categorized as 'evclass=128, evtype=3' with energies $0.1 \leq E \leq 300$ GeV γ-rays within a circular region of interest (ROI) of 15° centred on the source and with zenith angle 90° were extracted. The appropriate good time intervals were then generated by using the recommended criterion '(DATA_QUAL > 0)&&(LAT_CONFIG$==1$)'. The likely effects of cuts and selections, as well as the presence of other sources in the ROI, were incorporated by generating an exposure map on the ROI and an additional annulus of 15° around it with the third LAT catalogue (3FGL - gll_psc_v16.fit; Acero et al. 2015). We used the latest isotropic model, 'iso_P8R2_SOURCE_V6_v06', and the Galactic diffuse emission model 'gll_iem_v06'. To evaluate the significance of detection, we used the maximum-likelihood (ML) ratio test defined as $TS = 2\triangle \log(L)$, where L is the likelihood function between models with and without a γ-ray point source at the position of 3C 454.3 (Paliya, Stalin & Ravikumar 2015a). We considered the source as detected if TS > 9, which corresponds to a 3σ detection (Mattox et al. 1996). We generated the source light curve with a time binning of 1 d. For bins with TS < 9, the source was considered undetected. We arrived at a γ-ray light curve containing 2394 confirmed measurements. All the errors associated with *Fermi*-LAT points are the 1σ statistical uncertainties.

[1] http://fermi.gsfc.nasa.gov/ssc/data/analysis/documentation/

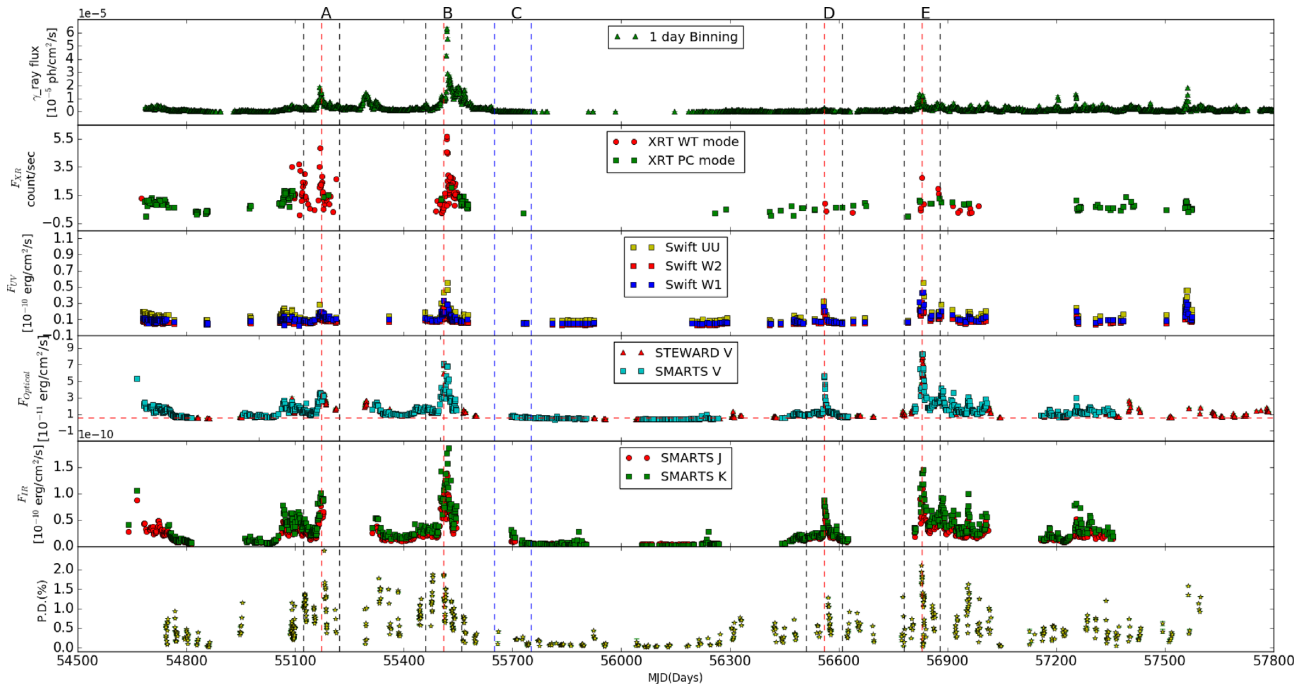

Figure 1. Multiwavelength light curve of the source 3C 454.3. From the top, the first panel shows the 1 d binned γ-ray light curve for the time range MJD 54500–57800. The second panel shows the *SWIFT*-XRT light curve in both PC (photon counting) and WT (window timing) modes. The third panel shows the *Swift* UVOT light curves in the W1, W2, and UU bands. In the fourth panel the optical light curve in the *V* band is given. The fifth panel shows the IR light curves in *J* and *K* bands and in the bottom panel variation of the degree of polarization is presented.The red vertical lines correspond to the peaks of the optical flares and the two black vertical lines denote a width of 50 d each on either side of the peak of the flare. The two vertical blue lines have a width of 100 d and correspond to the quiescent period.

2.2 X-ray data

For X-rays covering the energy range of 0.3–10 keV, we used the data from the X-ray Telescope (XRT; Burrows et al. 2005) onboard the *Swift* satellite (Gehrels et al. 2004) taken from the archives at HEASARC.[2] The data collected during the period 2008 August–2017 February were analysed with default parameter settings following the procedures given by the instrument team. For light-curve analysis, data collected using both window timing (WT) and photon counting (PC) modes were used; however, for spectral analysis only data collected from PC mode were used. The collected XRT data were processed with the XRTPIPELINE task using the latest CALDB files available with version HEASOFT-6.21. We used the standard grade selection 0–12. The calibrated and cleaned event files were summed to generate energy spectra. The source spectra were extracted from a circular region of radii 50 arcsec, whereas the background spectra were selected from a region of radii 55 arcsec. We combined the exposure map using the tool XIMAGE and ancillary response files created with xrtmkarf. We used an absorbed simple power-law model with the Galactic neutral hydrogen column density of $N_{\rm H} = 6.5 \times 10^{20}$ cm^{-2} from Kalberla et al. (2005) to perform the fitting within XSPEC (Arnaud 1996). We obtained 128 and 191 X-ray flux measurements at 0.3–10 keV in WT and PC mode, respectively.

2.3 UV–optical–NIR data

For UV and optical we used the data from the *Swift*-Ultraviolet/Optical Telescope (UVOT). We integrated *Swift*-UVOT data using the task `uvotimsum`. Source counts were extracted from a 5 arcsec circular region centred at the target and the background region was extracted from a larger area of a 10 arcsec nearby source-free region. The magnitude of 3C 454.3 was extracted using the task `uvotsource`. The magnitudes were not corrected for Galactic reddening. The estimated magnitudes were then converted to flux units using the zero points given in Breeveld et al. (2011). In addition to UVOT, optical data were also taken from SMARTS[3] (Small and Moderate Aperture Research Telescope System) as well as the Steward Observatory.[4] Similarly near-infrared (NIR) data in the *J* and *K* bands were taken from observations carried out using the ANDICAM instrument on the SMARTS 1.3 m telescope as part of a blazar monitoring campaign, supporting the *Fermi* multiwavelength AGN science. The details of the instrument and the data reduction procedures can be found in Bonning et al. (2012).

2.4 Optical polarization data

Optical polarization data in the *V* band were taken from Steward Observatory of the University of Arizona. Details of the data and its reduction based on spectropolarimetric observations can be found in Smith et al. (2009). The polarization data available from Steward observatory and covering the period 2008 August to 2017 February consisted of 644 measurements. The optical polarization data along with flux measurements in other wavebands are shown in Fig. 1.

[2] https://heasarc.gsfc.nasa.gov/docs/archive.html

[3] http://www.astro.yale.edu/smarts/glast/home.php

[4] http://james.as.arizona.edu/~psmith/Fermi

Table 1. Details of the epochs considered for light curves, SED and spectral analysis. Here, 'ID' refers to the epochs. The γ-ray fluxes are in units of 10^{-6} ph cm^{-2} s^{-1} and the optical fluxes are in units of 10^{-11} erg cm^{-2} s^{-1}.

	MJD		Calendar date		Mean flux	
ID	Start	End	Start	End	γ	Opt.
A	55122	55222	2009-10-18	2010-01-26	4.97	1.76
B	55460	55560	2010-09-21	2010-12-30	11.7	2.81
C	55650	55750	2011-03-30	2011-07-08	0.54	0.68
D	56510	56610	2013-08-06	2013-11-14	0.99	1.67
E	56780	56880	2014-05-03	2014-08-11	3.75	3.23

3 ANALYSIS

3.1 Multiwavelength light curves

The multiwavelength light curves that include γ-ray, X-ray, UV, optical, and IR along with the polarization measurements from 2008 August to 2017 February (MJD: 54500–57800) are shown in Fig. 1. From Fig. 1 it is evident that 3C 454.3 has gone through both quiescent and active phases during the period MJD 54500–57800. During this period, we identified four time intervals during which large optical flares were seen. They are denoted by epochs A, B, D, and E and cover the period MJD 55122–55222 (epoch A), MJD 55460–55560 (epoch B), MJD 56510–56610 (epoch D), and MJD 56780–56880 (epoch E). The above four intervals were chosen such that (i) there is a gradual increase of the optical brightness at least by 0.5 mag from the quiescent level, (ii) there is a corresponding declining branch from the peak back to the quiescent level, and (iii) the rising and decaying phases (both inclusive) last for more than 50 d. The peaks of the flares are shown as a vertical dashed red line in Fig. 1. On either side of the red lines are two black vertical lines, having a total duration of 100 d. We also identified a time interval denoted as 'epoch C' and covering the period MJD 55650–55750, where the source was at its quiescent state in IR, optical, UV, X-rays, and γ-rays. This quiescent period for a duration of 100 d is indicated by two vertical blue lines in Fig. 1. The details of the five epochs that were identified for further analysis along with their mean optical and γ-ray flux levels are given in Table 1. Detailed analyses of each of these five epochs are given in the following sub-sections.

3.1.1 Epoch A (MJD 55122–55222)

An inspection of Fig 1. indicates that there is a close correlation between IR, optical, UV, X-rays, and γ-rays. Optical polarization data, though sparse during this period, were not available during the peak of the flare, making it impossible to comment on the nature of the optical polarization during the peak of the γ-ray flare. The multiband light curves covering for a duration of 100 d centred on the peak of epoch A, along with the polarization measurements when available, are given in Fig. 2.

To check for the presence of any correlation between optical and γ-ray flux variations we cross-correlated the optical and γ-ray light curves using the discrete correlation (DCF) technique of Edelson & Krolik (1988) and the interpolated cross-correlation function (ICCF) technique of Gaskell & Sparke (1986) and Gaskell & Peterson (1987) . The errors in both DCF and ICCF were obtained by carrying out a Monte Carlo analysis that involves both flux randomization and random subset selection following the procedures outlined in Peterson et al. (2004) . The results of the cross-correlation function analysis are shown Fig. 3 both for ICCF and DCF. The lag was determined by the centroid of the cross-correlation function, which includes all points within 80 per cent of the peak of the cross-correlation function. We found a lag of $2.2^{+0.9}_{-0.9}$ d with the γ-ray leading the optical flux variations. This is similar to the lag of about 4 d found between the γ-ray and optical band by Gaur, Gupta & Wiita (2012) on analysis of the data for the time period 2009 November to 2009 December. However, Gupta et al. (2017) found that the optical and γ-rays are correlated with zero lag during the period MJD 55150–55200, which is within the range analysed here. During the same period, Gupta et al. (2017) found that during the declining phase of the γ-ray flare, the degree of optical polarization increased, showing a clear signature of anticorrelation between γ-ray flux variation and optical polarization.

3.1.2 Epoch B (MJD 55460–55560)

During this period, the peak of the optical flare is about two times larger than the peak of the optical brightness at epoch A. The γ-ray brightness too peaked at nearly the same time as the optical flare. During this epoch, visual inspection indicates close correlation between γ-ray, X-ray, UV optical, and IR flux variations. During this period a short-duration intense flare in the optical was observed superimposed on the large optical flare at around MJD 55510. This particular short-duration optical flare has no corresponding γ-ray flare (Fig. 4) and is thus a case of an optical flare with no corresponding γ-ray counterpart. At the epoch of this short-duration optical flare, there is also enhanced optical polarization, pointing to a strong correlation between optical flux and polarization variations. At this time, enhanced flux levels were also seen in UV and X-ray bands. This remarkable short-duration intense optical flare with no corresponding flare in the gamma band was also noticed by Vercellone et al. (2011). According to Vercellone et al. (2011) this optical flare showed a sharp rise and decay in 48 h. At the same time, a 20 per cent rise was seen in the X-ray with no change at other wavelengths. During the duration of the large optical flare with the peak at MJD 55519, data on the degree of optical polarization are missing to make any statement on the correlation or anticorrelation between the optical flux and polarization variations. DCF and ICCF analysis between optical and γ-ray flux variations, shown in Fig. 5, indicate that the time delay between optical and γ-ray flux variations is $0.8^{+1.1}_{-1.0}$. Thus, during this major optical flare in epoch B, the optical and γ-ray flux variations are correlated with zero lag.

3.1.3 Epoch D (MJD 56510–56610)

The optical flux during this epoch has nearly the same amplitude as the optical flare at epoch B. Considering the correlation between optical and γ-ray flux variations during both epochs A and B, it is natural to expect the γ-ray flare at epoch D to have similar brightness to that of epoch B. However, the source was barely detected in the γ-ray band during this period. This is an indication of an optical flare with no/weak corresponding γ-ray flare (Fig. 6). Correlation analysis between the optical and γ-ray light curves during this epoch gives a time delay of $1.0^{+0.7}_{-0.5}$ d. This shows that the optical and the very weak γ-ray variations are correlated with 1 d lag. The results of the cross-correlation function analysis are shown in Fig. 7. Polarization data were not available during the period of the flare and therefore the correlation if any between optical flux and polarization variations could not be ascertained.

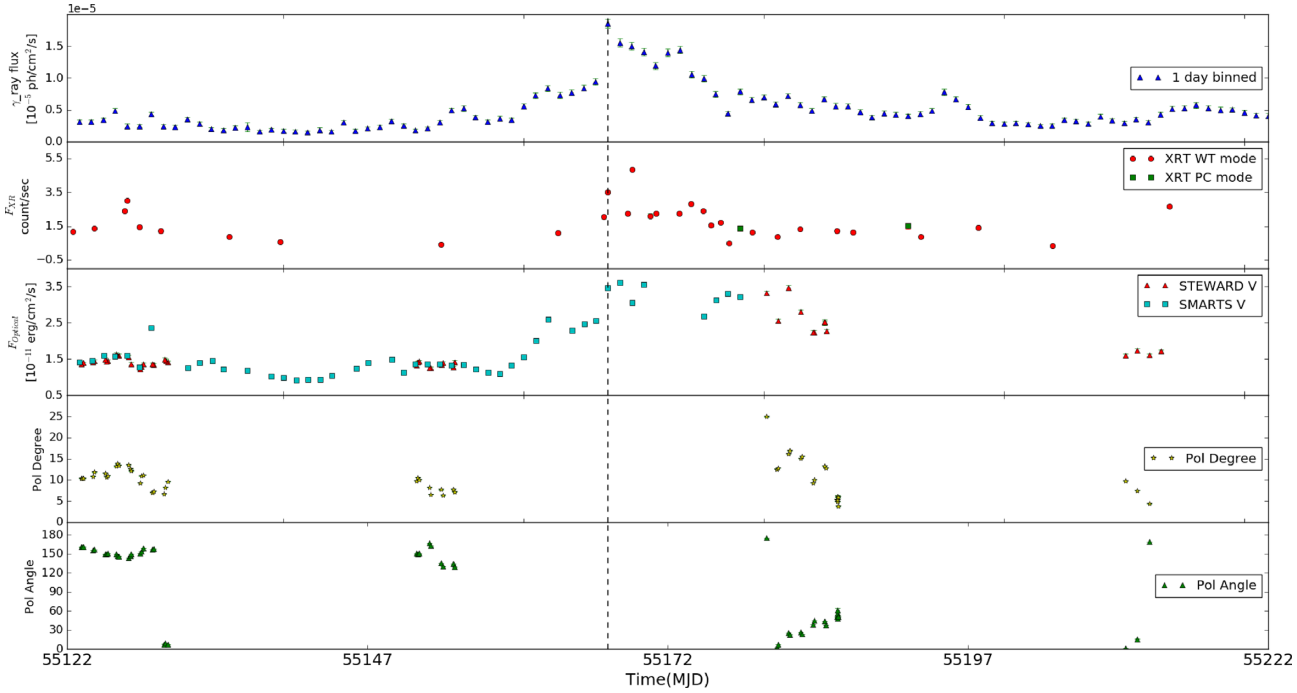

Figure 2. Multiwavelength light curves covering a period of 100 d during epoch A. Here, from the top the first panel shows the γ-ray variations, the second and third panels show the variations in X-ray and optical bands, and the bottom two panels show the variations in degree of optical polarization and polarization position angle.

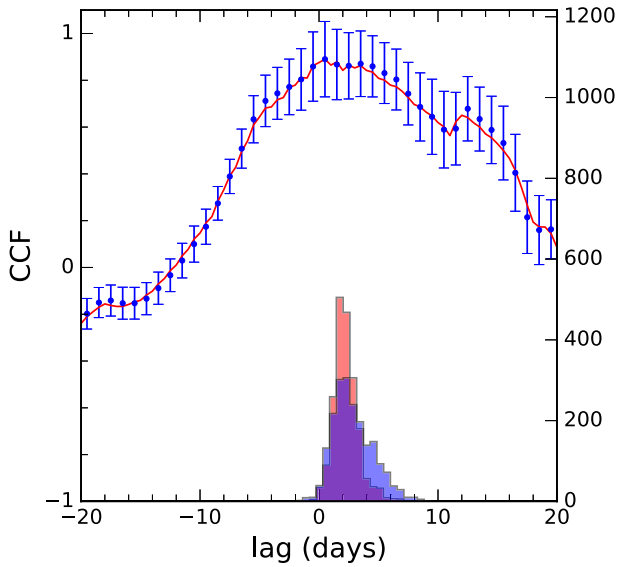

Figure 3. Cross-correlation analysis between γ-ray and optical flux variations during epoch A. The solid line is for ICCF and the filled circles refer to DCF. The histograms in blue and orange show the distribution of cross-correlation centroids for ICCF and DCF, respectively.

3.1.4 Epoch E (MJD 56780–56880)

During this epoch the optical flare has a peak brightness similar to that of the optical flare at epoch B, but the source has minor γ-ray flare during this epoch. This same period was also independently analysed by Kushwaha et al. (2017) for correlation between γ-ray and optical flux variations. They find no lag between optical and γ-ray flux variations during the period overlapping the duration of epoch E. Our correlation analysis between the optical and γ-ray light curves during this epoch gives a time delay of $0.3^{+0.7}_{-0.5}$ d. Correlation analysis for this epoch shown in Fig. 9. We noticed an interesting feature by careful examination of the optical total flux and polarization variations shown in Fig. 8. The degree of optical polarization is anticorrelated with the optical flare during both the rising phase and the decaying phase of the flare. Though such anticorrelations between optical flux and polarization variations were known before in the blazar BL Lac (Gaur et al. 2014) and 3C 454.3 (Gupta et al. 2017), we noticed anticorrelation between optical flux and polarization variations during both the rising part of the flare and the decaying part of the flare.

3.2 Spectral variations

To check for any spectral variation in the optical/IR bands, we looked for variation in the $V - J$ band colour against the V-band brightness. This colour variation was analysed for the epochs A, B, D, and E. During epochs A and B, the source showed a 'redder when brighter' (RWB) behaviour. During epoch E, a bluer when brighter behaviour was observed. During epoch D, we observed a complex behaviour. Upto a V-band brightness of around 15 mag, the source showed a 'bluer when brighter' behaviour, but for optical brightness fainter than 15.0 mag, a 'redder when brighter' behaviour was observed. The colour–magnitude diagrams for all the four epochs are shown in Fig. 10. The spectral variations shown by the source are thus complex. From studies on the optical–IR colour–magnitude diagram, it is known that FSRQs in general show an RWB trend, which is attributed to them having a luminous accretion disc (Gu et al. 2006; Bonning et al. 2012). The observed optical emission is a combination of thermal blue emission from the accretion disc and non-thermal red emission from the jet. As the source gets brighter, the non-thermal emission has a more dominant contribution to

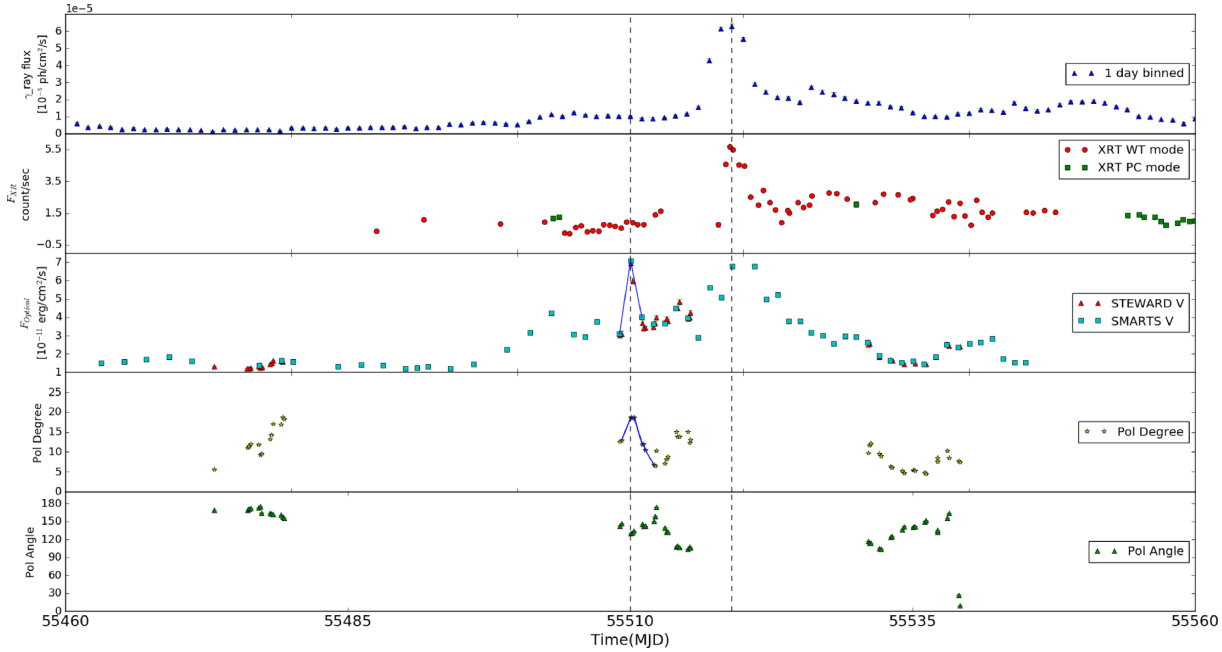

Figure 4. Multiwavelength light curves for a duration of 100 d during epoch B. The panels have the same meanings as those of Fig. 2.

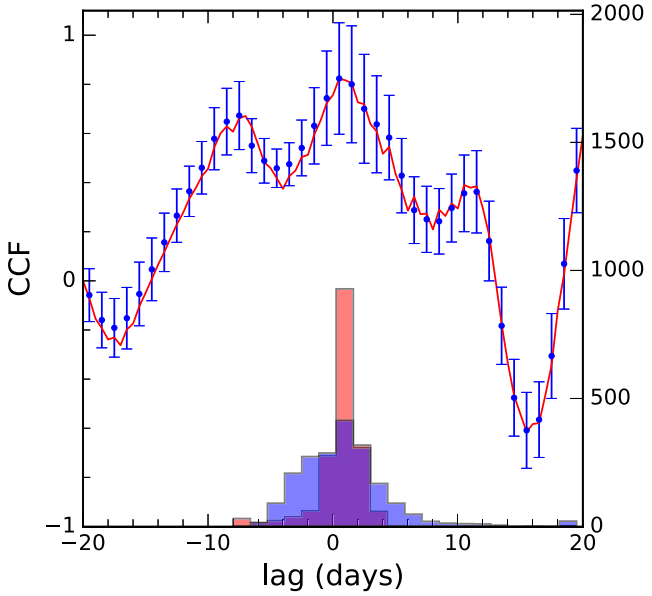

Figure 5. Cross-correlation analysis between γ-ray and optical flux variations during the major flare in epoch B. The solid line is for ICCF and the filled circles refer to DCF. The histograms in blue and orange show the distribution of cross-correlation centroids for ICCF and DCF, respectively.

the total flux, giving rise to the RWB behaviour (Bonning et al. 2012). During epochs A and B, there is a trend of the object to become RWB, irrespective of its optical brightness. The optical flares dominated by synchrotron emission processes during A and B have corresponding γ-ray flares that are produced by EC processes. However, during epochs D and E, the colour variations were found to depend on the optical brightness. During the epochs when this complex spectral behaviour was noticed, the source showed an optical/IR flare with no or a weak corresponding flare in the γ-ray band. The source showed a much larger amplitude of variability in the optical/IR bands, while in the γ-ray band it was either faint or below the detection limit of *Fermi*. This definitely points to some complex physical changes and could be due to a combination of changes in the bulk Lorentz factor, electron energy density, and magnetic field as seen from our SED modelling of the multiband data.

3.3 γ-ray spectra

The shape of the γ-ray spectrum can provide evidence on the intrinsic distribution of electrons involved in the γ-ray emission processes that might involve acceleration and cooling processes. For all the five intervals identified above, we generated the γ-ray spectra and fitted them with two models, namely a simple power-law (PL) model and a log parabola (LP) model. The PL model has the form

$$\mathrm{d}N(E)/\mathrm{d}E = N_\circ(E/E_\circ)^{-\Gamma}, \quad (1)$$

where $N_\circ$ is normalization of the energy spectrum and $E_\circ$ = 300 MeV, which is constant for all SEDs.

The LP model is defined as below following Nolan et al. (2012)

$$\mathrm{d}N(E)/\mathrm{d}E = N_\circ(E/E_\circ)^{-\alpha-\beta ln(E/E_\circ)}. \quad (2)$$

Here, dN/dE is the number of photons cm^{-2} s^{-1} MeV^{-1}, α is the photon index at $E_\circ$, β is the curvature index, E is the γ-ray photon energy, and $N_\circ$ and $E_\circ$ are the normalization and scaling factor of the energy spectrum, respectively.

We used the maximum likelihood estimator gtlike for spectral analysis likelihood ratio test (Mattox et al. 1996) to check the PL model (null hypothesis) against the LP model (alternative hypothesis). $\mathrm{TS_{curve}} = 2(\log L_{\mathrm{LP}} - \log L_{\mathrm{PL}})$ was also calculated (Nolan et al. 2012). The presence of a significant curvature was tested by setting the condition $\mathrm{TS_{curve}} > 16$. γ-ray spectra for these five epochs are shown in Fig. 11 and the results of the γ-ray spectral analysis are shown in Table 2. On all the five epochs the γ-ray spectra is well fitted with an LP model.

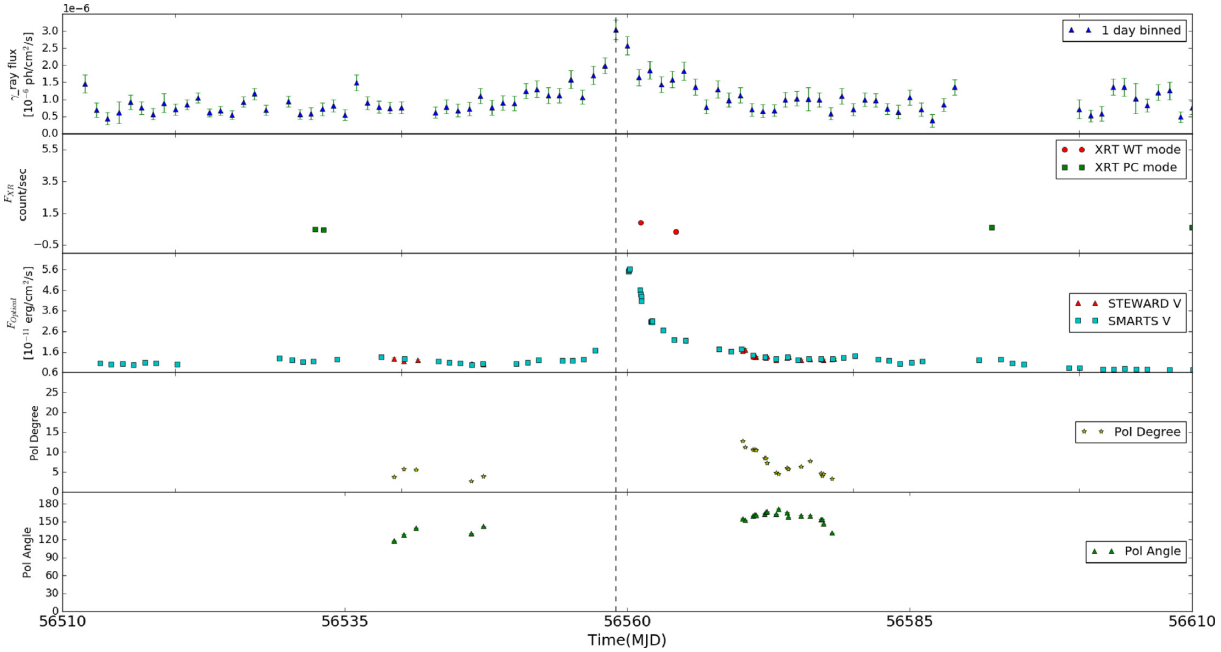

Figure 6. Multiwavelength light curves in γ-rays, X-ray, and optical for a period of 100 d during epoch D. The degree of optical polarization and polarization position angles are shown in the bottom two panels.

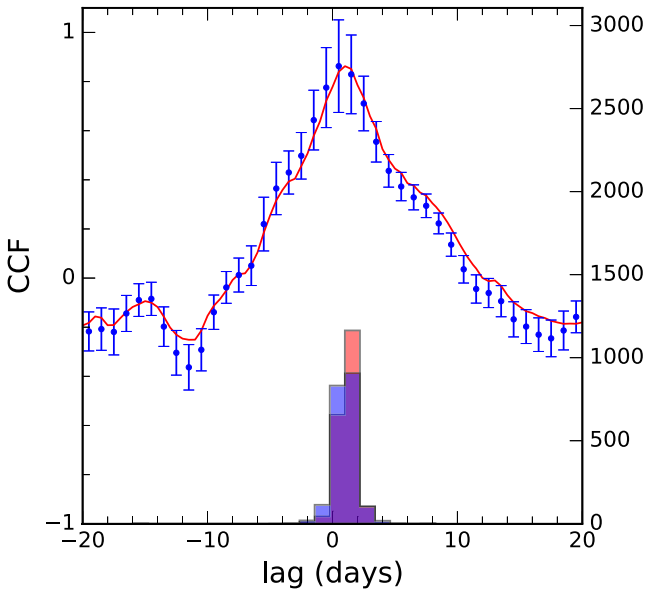

Figure 7. Correlation between optical and γ-ray flux variations during epoch D. The solid line and filled circles refer to the ICCF and DCF, respectively. The distribution of the cross-correlation centroids obtained using ICCF and DCF are shown in blue and orange, respectively.

3.4 Spectral energy distribution modelling

To characterize the nature of the source during epochs A, B, C, D, and E, we constructed the broad-band spectral energy distribution. For UV, optical, and IR, all data points over the 100 d period in each of the epochs were averaged filter-wise to get one data point for each filter. However, for X-ray and γ-rays, all the available data over the 100 d period in each of the epochs were used to construct their average spectra. All the generated SEDs were modelled using the one-zone leptonic model of Sahayanathan & Godambe (2012). In this model, the emission region is assumed to be a spherical blob of size R filled with non-thermal electrons following a broken power-law distribution

$$N(\gamma)\,\mathrm{d}\gamma = \begin{cases} K\,\gamma^{-p}\,\mathrm{d}\gamma & \text{for} \quad \gamma_{\rm min} < \gamma < \gamma_{\rm b} \\ K\,\gamma_{\rm b}^{q-p}\gamma^{-q}\,\mathrm{d}\gamma & \text{for} \quad \gamma_{\rm b} < \gamma < \gamma_{\rm max} \end{cases} \tag{3}$$

where γ is the electron Lorentz factor and p and q are the low- and high-energy power-law indices with $\gamma_{\rm b}$ the Lorentz factor corresponding to the break energy. The emission region is permeated with a tangled magnetic field B and move down the jet with a bulk Lorentz factor Γ. The broad-band SEDs are modelled using synchrotron, SSC, and EC emission mechanisms. This model was added as a local model in XSPEC (Arnaud 1996) and the source parameters were obtained through χ^2 minimization (Sahayanathan, Sinha & Misra 2018). The observed spectrum is mainly governed by 10 free parameters, with 4 of them governing the electron distribution, namely, p, q, $\gamma_{\rm b}$, and the electron energy density $U_{\rm e}$. The rest of the six parameters are B, R, Γ, the jet viewing angle θ, the temperature of the external thermal photon field T, and the fraction of the external photons taking part in the EC process, f. To account for the model-related uncertainties, we added 12 per cent systematic error evenly over the entire data. For SED model fits, corrections due to galactic absorption were applied to the IR, optical,[5] UV (Raiteri et al. 2011), and X-ray data points.

To investigate the difference in the flaring behaviour of the source during various epochs, the SED-fitting methodology was carried out in the following manner. First, the typical value of the source parameters governing the observed broad-band emission from 3C 454.3 was attained by fitting the quiescent state C. The limited information available through optical, X-ray, and γ-ray observations did not let us constrain all the parameters. The information that could be obtained from the observed SEDs was the high-energy and low-

[5] http://ned.ipac.caltech.edu

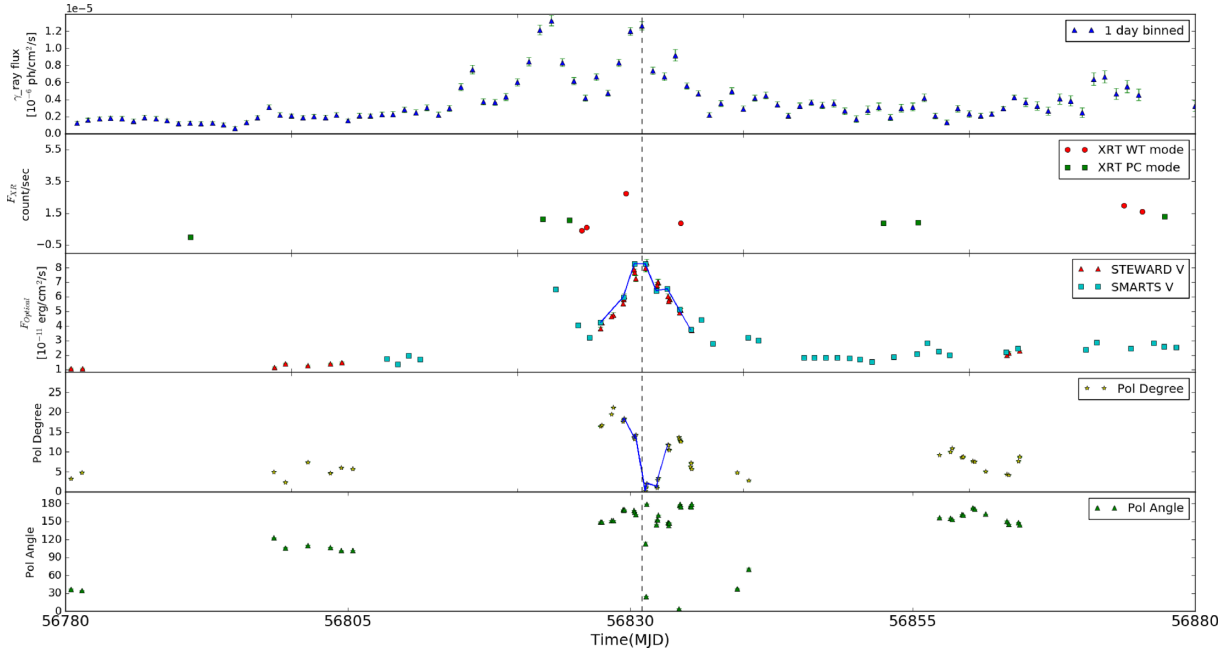

Figure 8. Multiwavelength flux and polarization variations during epoch E.

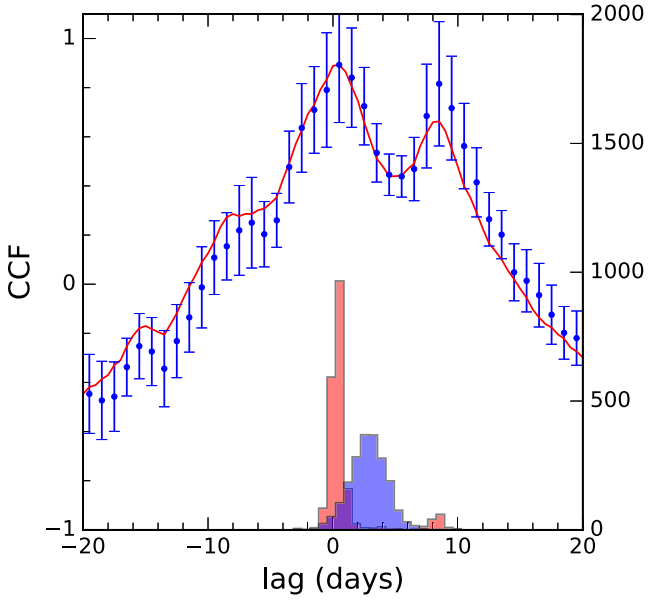

Figure 9. Correlation between optical and γ-ray flux variations during epoch E. The solid line and filled circles refer to the ICCF and DCF, respectively. The distribution of the cross-correlation centroids obtained using ICCF and DCF are shown in blue and orange, respectively.

energy spectral indices, synchrotron flux at optical, SSC flux at X-ray, and EC flux at γ-ray energies. Consistently we chose five parameters, namely, p, q, U_e, B, and Γ to be free and froze the rest of the parameters. Details of the parameters are given in Table 3. The values of γ_{min}, γ_{max}, and θ were chosen to be 40, 10^4, and 1°, respectively. The other parameters have $R = 3 \times 10^{15}$, $T = 1000$ K, $f = 0.90$. The adopted size of the γ-ray-emitting region has been found from a gravitational microlensing effect that ranges from 10^{14} to 10^{15} cm (Vovk & Neronov 2016). The resultant best-fitting parameters for epoch C are given in Table 3 and the model SED with the observed one is shown in Figs 12 and 13.

The fitting procedure was repeated for the epochs A, B, and D with the choice of free parameters similar to the case of epoch C. For epochs A and B, where optical and γ-ray flares are correlated, we found the main difference is seen in the enhancement of the bulk Lorentz factor and a marginal decrease in the magnetic field. For epoch A, the increase in the bulk Lorentz factor is relatively less; however, this is also associated with an increase in electron energy density. On the other hand, for epoch D with an isolated orphan optical flare, we found the SED can be reproduced with an increase in the bulk Lorentz factor and magnetic field and decrease in the electron energy density relative to the quiescent epoch C. For epoch E, where a major flare is observed in optical compared to γ-ray, we found the SED cannot be reproduced satisfactorily with the parameters similarly to epoch C; rather it demands a large emission region size with a low Lorentz factor. Hence, the emission region during this epoch may be at large jet scale where the jet cross-section is significantly larger. During all the epochs, we also observed the variations in the high- and low-energy particle power-law indices and this can also manifest the flux variations observed at these energies. Our modelling also shows that the observed broad-band SED over all the epochs can be well described by the leptonic scenario (Figs 12 and 13).

4 RESULTS AND DISCUSSION

4.1 γ-ray spectra

The γ-ray spectra of 3C 454.3 in all the five epochs considered here that include both the active and quiescent phases are well described by the LP model. Such a curved γ-ray spectrum is generally seen in FSRQs (Abdo et al. 2010a). In the third catalogue of AGNs detected by *Fermi* LAT, the spectrum of 3C 454.3 is well described by a power law with an exponential cut-off model (Ackermann et al. 2015). Such an observed curved γ-ray spectrum could be

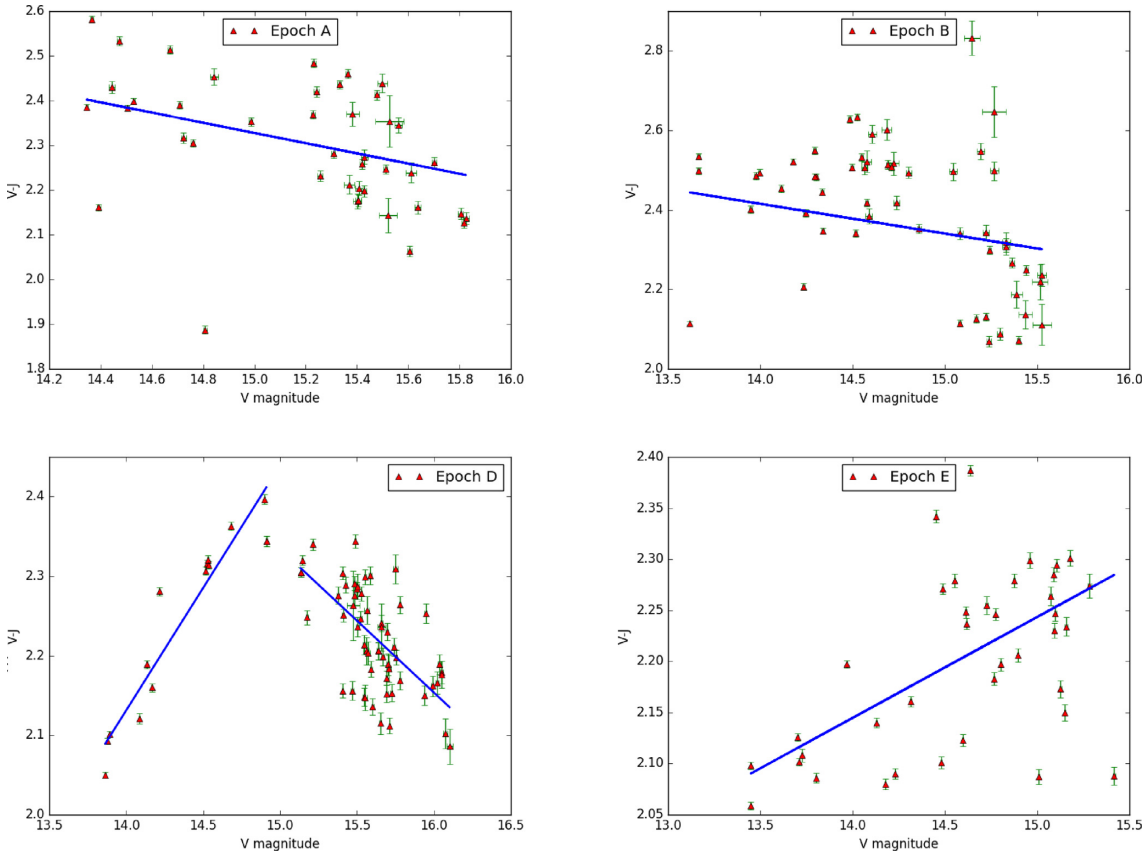

Figure 10. Colour–magnitude relations for epochs A, B, D, and E.

due to the electrons giving rise to the emission having a curved energy distribution (Dermer et al. 2015). Alternatively, the curved γ-ray spectrum is a manifestation of the attenuation of high-energy γ-rays through photon–photon pair production (Coogan, Brown & Chadwick 2016). The parameter α in the LP model is a measure of the slope of the γ-ray spectrum, with a small value of α indicating a harder γ-ray spectrum. The curvature parameter β gives a measure of the presence of cut-off in the spectrum at high energies with a large value of β indicating a sharper cut-off. Therefore, investigation of any changes in the values of α and β parameters during the five epochs can point to changes in the γ-ray spectral shape. A change in the γ-ray spectral parameters during a flaring state could point to a change in the position of the γ-ray-emitting region. The variation of the α and β against flux during the five epochs studied here is shown in Fig. 14. No trend on the variation of α with flux was seen during the five epochs considered here. However, a plot of β with flux (Fig. 14) shows a clear trend of a decrease in the curvature parameter with increasing flux. Linear least-squares fit to the data gives $\beta = (-0.005 \pm 0.009)F_V + (0.168 \pm 0.029)$ with a correlation coefficient of -0.77. Clearly the value of β is high and low at the lowest and the highest flux levels among the five epochs analysed here. Such a trend is also seen by Ackermann et al. (2015) on analysis of the FSRQs in the third catalogue of AGNs detected by *Fermi* (3LAC). The changes in the γ-ray spectral shape during different brightness states of 3C 454.3 could point to the emission site located at different regions during different brightness states; however, other explanations could not be ruled out. Studies on the flares of 3C 454.3 in December 2009 and November 2010 that fall in the epochs A and B studied here concluded that the γ-ray emission regions were located close to the central black hole (Jorstad et al. 2012; Isler et al. 2013).

4.2 Connection between optical and GeV flux variations

In a majority of the multiwavelength monitoring observations of blazars, close correlations between the flux variations in different bands were noticed (Bonning et al. 2009). This was explained on the co-spatiality of the emission regions emitting in different bands and the correlated optical and GeV flux variations can be understood in the standard leptonic emission processes according to which the same relativistic electrons produce optical and γ-ray emission via synchrotron and IC processes. However, there are a handful of blazars where the emission in the optical and GeV γ-ray bands are found not to be correlated (Chatterjee et al. 2013a; Dutka et al. 2013; Cohen et al. 2014; MacDonald et al. 2015). During the 9 yr of monitoring data analysed here we found four flaring epochs in the optical, namely A,B, D, and E. During epochs A and B, the optical flare is accompanied by a γ-flare, while at the other two epochs D and E, though the optical flares have amplitudes similar to those of epochs A and B, the γ-rays during epochs D and E were either weak or undetected. This is clearly seen in Fig. 15, where the logarithm of γ-ray flux is plotted against the logarithm of optical flux. The results of the linear least-squares fit carried out between the γ-ray flux F_γ and optical flux in the V-band F_V during those four epochs yielded the following relations given in equations (4)–(7) for epochs A, B, D, and E, respectively. The results of the fit are given in Table 4.

$$\log F_\gamma^{\rm A} = (1.528 \pm 0.112) \log F_V^{\rm A} + (11.128 \pm 1.190) \quad (4)$$

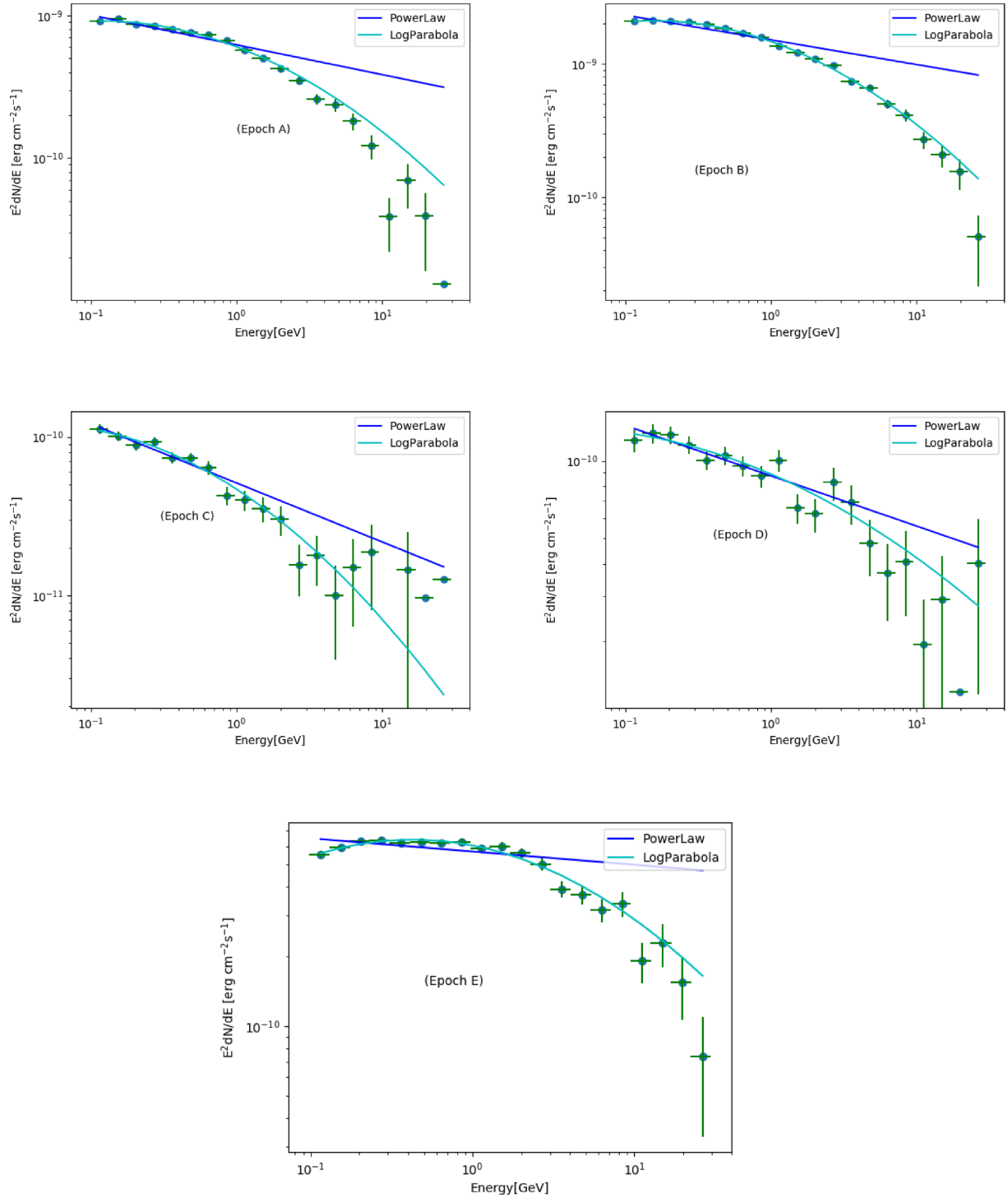

Figure 11. Simple power-law and log parabola fits to the γ-ray spectra of 3C 454.3 during epochs A, B, C, D, and E.

$$\log F_{\gamma}^{\mathrm{B}} = (1.017 \pm 0.144) \log F_{V}^{\mathrm{B}} + (5.945 \pm 1.506) \quad (5)$$

$$\log F_{\gamma}^{\mathrm{D}} = (0.561 \pm 0.048) \log F_{V}^{\mathrm{D}} + (0.132 \pm 0.510) \quad (6)$$

$$\log F_{\gamma}^{\mathrm{E}} = (0.974 \pm 0.068) \log F_{V}^{\mathrm{E}} + (4.901 \pm 0.706). \quad (7)$$

The above equations clearly indicate that when the source showed optical flares during epochs D and E, the γ-ray emission was weak. Thus, during these two epochs there is a clear case of optical flares with weak/no-corresponding γ-ray counterparts. Also during epoch B, prior to the large optical flare with a counterpart in the γ-ray band, a short-duration and intense optical flare was found around MJD 55510, without a γ-ray counterpart, also only noticed by Vercellone et al. (2011). According to Vercellone et al. (2011) such a lack of a simultaneous γ-ray at MJD 55510 could be due to either

Table 2. Details of the PL and LP model fits for five epochs. Here the γ-ray flux value is in units of 10^{-6} ph cm^{-2} s^{-1}.

	PL				LP					
Epochs	Γ	Flux	TS	−Log L	α	β	Flux	TS	−Log L	TS$_{curve}$
A	− 2.34 ± 0.01	5.68 ± 0.06	87 024.8	138 177.8	1.91 ± 0.03	0.15 ± 0.01	4.93 ± 0.07	79 568.2	137 962.7	430.1
B	− 2.33 ± 0.01	13.3 ± 0.08	278 585.0	80 508.1	2.21 ± 0.00	0.09 ± 0.00	12.79 ± 0.12	283 811.0	80 238.2	539.8
C	− 2.42 ± 0.03	0.57 ± 0.02	3422.6	151 787.4	1.97 ± 0.10	0.24 ± 0.04	0.47 ± 0.03	3392.8	151 756.9	61.0
D	− 2.25 ± 0.02	1.03 ± 0.03	9890.6	142 338.0	2.04 ± 0.04	0.14 ± 0.02	0.88 ± 0.03	9768.6	142 299.7	76.6
E	− 2.14 ± 0.00	4.42 ± 0.00	66161.9	146 140.9	1.53 ± 0.00	0.15 ± 0.00	3.71 ± 0.03	62 145.3	145 896.2	489.4

Table 3. Details of the SED fitting using XSPEC.The other adopted parameters for epochs A, B, C, and D are $\gamma_{min} = 40$, $\gamma_{max} = 10^4$, $R = 3 \times 10^{15}$ cm, $T = 1000$ K, $\gamma_b = 1200$, and $f = 0.90$. The parameters for epoch E are $\gamma_{min} = 40$, $\gamma_{max} = 4.0 \times 10^4$, $R = 9 \times 10^{16}$ cm, $T = 800$ K, $\gamma_b = 1500$, and $f = 0.80$.

Parameters	Epoch A	Epoch B	Epoch C	Epoch D	Epoch E
Bulk Lorentz factor	11.79 ± 0.82	16.63 ± 0.96	7.30 ± 0.30	11.88 ± 1.07	5.00 ± 0.71
Low-energy particle index	1.47 ± 0.16	1.34 ± 0.13	1.56 ± 0.09	1.98 ± 0.15	1.37 ± 0.11
High-energy particle index	3.64 ± 0.11	3.93 ± 0.09	3.12 ± 0.11	3.49 ± 0.15	3.14 ± 0.08
Electron energy density (cm^{-3})	5.15 ± 1.08	2.05 ± 0.36	3.62 ± 0.32	1.15 ± 0.24	0.04 ± 0.01
Magnetic field (Gauss)	1.77 ± 0.11	1.78 ± 0.09	2.82 ± 0.16	4.01 ± 0.23	0.73 ± 0.03
Chi-square/dof	1.0	1.0	0.84	1.30	1.07

enhancement of the magnetic field or attenuation by γ–γ production or lack of external seed photons. However, based on arguments from modelling Vercellone et al. (2011) indicate that the complex behaviour seen during epoch B could be due to changes in the external photon field. However, according to Vittorini et al. (2014) the anomalous flux variability patterns between optical and γ-ray can be due to inverse Compton scattering or process happening as the jet collides on to mirror cloud situated at parsec scales. Thus, the variability shown by 3C 454.3 in different energy bands is complex. To gain an insight into this anomalous variability behaviour we fitted the broad-band SED of the source in all the five epochs using simple one-zone leptonic emission models. During epochs A and B, where the optical and γ-ray flux variations are correlated, there is enhancement in the bulk Lorentz factor relative to the quiescent epoch C. During epoch D, we found an enhancement of the magnetic field related to the quiescent state C, which could explain the high optical flare accompanied by a very weak γ-ray flare. Such a change in magnetic field could also produce enhanced optical polarization and X-ray flux. But, the non-availability of optical polarization and X-ray flux measurements during epoch D precludes us from making a firm conclusion on the enhancement of the magnetic field as the cause for the occurrence of the optical flare with a weak γ-ray flare during epoch D; however, that is the most favourable scenario. In epoch E, where there is an optical flare with a weak γ-ray counterpart, our SED modelling indicates decrease in the electron energy density, magnetic field, and bulk Lorentz factor and also the emission region could be located at a region farther than the emission region of other epochs. We therefore conclude that the observations of an optical flare with a weak/no corresponding γ-ray flare during epochs D and E could be due to one or a combination of parameters such as the bulk Lorentz factor, magnetic field, and electron energy density or due to changes in the locations of the γ-ray-emitting regions. 3C 454.3 is the fourth blazar known to have shown the anomalous variability behaviour of optical flares with no γ-ray counterparts. The other sources where such behaviour was noticed are PKS 0208−512 (Chatterjee et al. 2013a), S4 1849+67 (Cohen et al. 2014), and 3C 279 (Pati no-Álvarez et al. 2018). A possible cause for optical flux variations without γ-ray counterparts could be attributed to hadronic processes (Mücke & Protheroe 2001); however, based on our SED analysis, we conclude that the leptonic model is also capable of explaining the emission from 3C 454.3 during all the epochs.

4.3 Correlation between optical flux and polarization

During epoch B, there is one short-term optical flare at around 55510 MJD. During this period there is no γ-ray flare. This intense short-duration optical flare without any γ-ray counterpart was also reported by Vercellone et al. (2011). Such an increased optical flare without any γ-ray counterpart can be due to magnetic field enhancement. In this scenario an increase in the magnetic field will lead to increased optical flare (from synchrotron process) and no increased γ-ray emission as the γ-ray emission from an inverse Compton process is independent of the magnetic field (Vercellone et al. 2011; Chatterjee, Nalewajko & Myers 2013b). Alternatively, the lack of a γ-ray flare coinciding with an optical flare at around 55510 MJD could be due to the attenuation of γ-rays via pair production or lack of an external photon field (Vercellone et al. 2011). Polarization observations can play a key role in arriving at a possible scenario for the anomalous flare seen at MJD 55510. During this time sparse polarization observations were available to make any analysis on the correlation between flux and polarization variations possible. The degree of polarization seems to be positively correlated with the optical flux change (Fig. 4), with the increase in the degree of polarization coinciding with the optical flare. Near simultaneous polarization observations were also available for epoch E. During this epoch, we have sufficient photometric observations to study the correlation between the degree of polarization and flux changes. The degree of polarization is found to be anticorrelated to the flux changes in the optical V band, during both the rising phase and the declining phase of the optical flare evident in Fig. 8. Such an anticorrelation between degree of optical polarization and total flux has been known before in the BL Lacertae object BL Lac (Gaur et al. 2014) and the FSRQ 3C 454.3 (Gupta et al. 2017). Such an anticorrelation between flux and degree of polarization could be explained in a two-component model consisting of a slowing varying component and a variable component with different polarization directions.

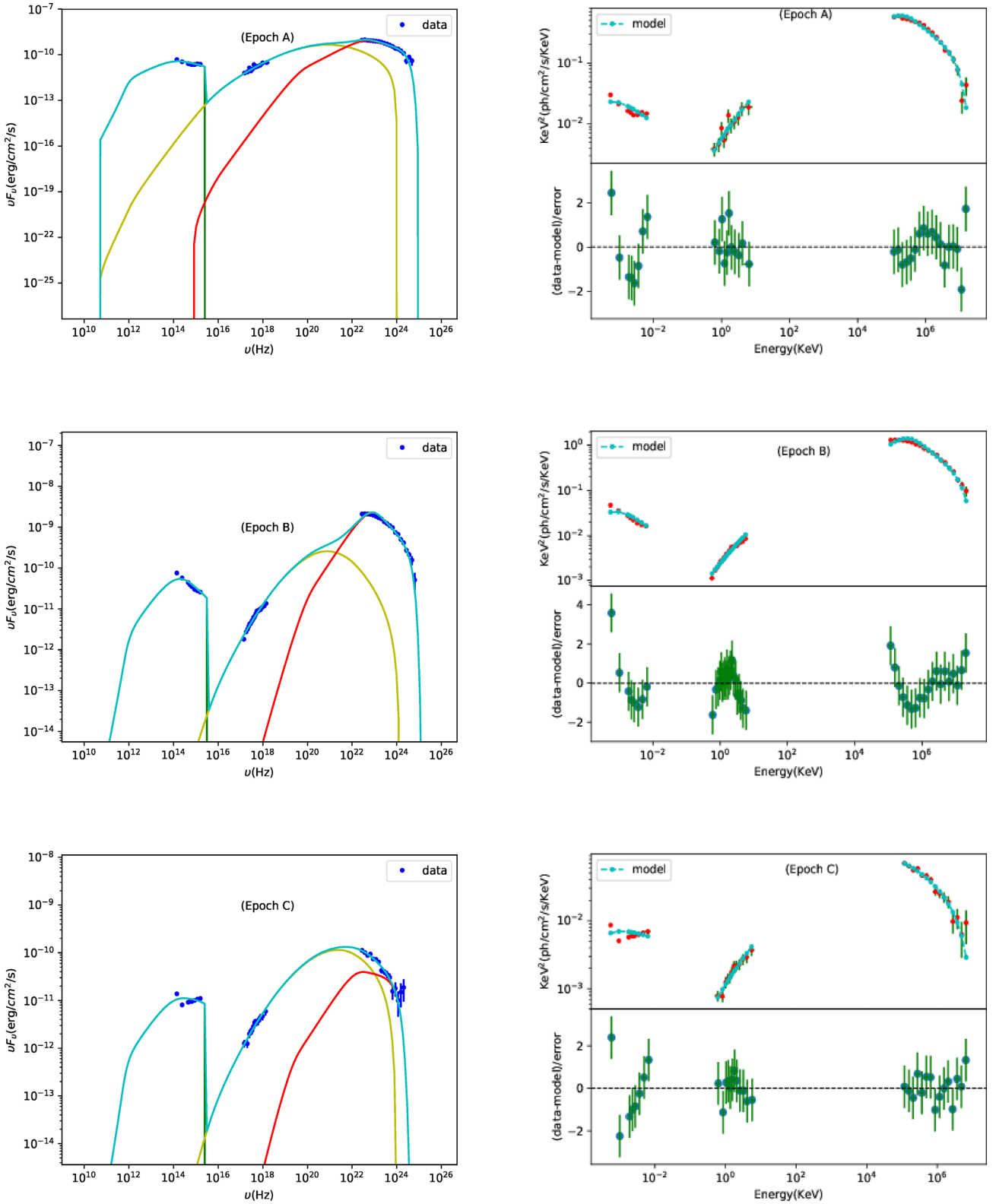

Figure 12. Broad-band spectral energy distribution along with the one-zone leptonic emission model fits for epochs A, B, and C. In the left-hand panels the green line refers to the synchrotron model, the yellow line refers to the SSC process, and the red line refers to the EC process. The cyan line is the sum of all the components. In the right-hand panels for each epoch the first panel shows the fitting of the model to the data carried out in XSPEC and the second panel shows the residuals.

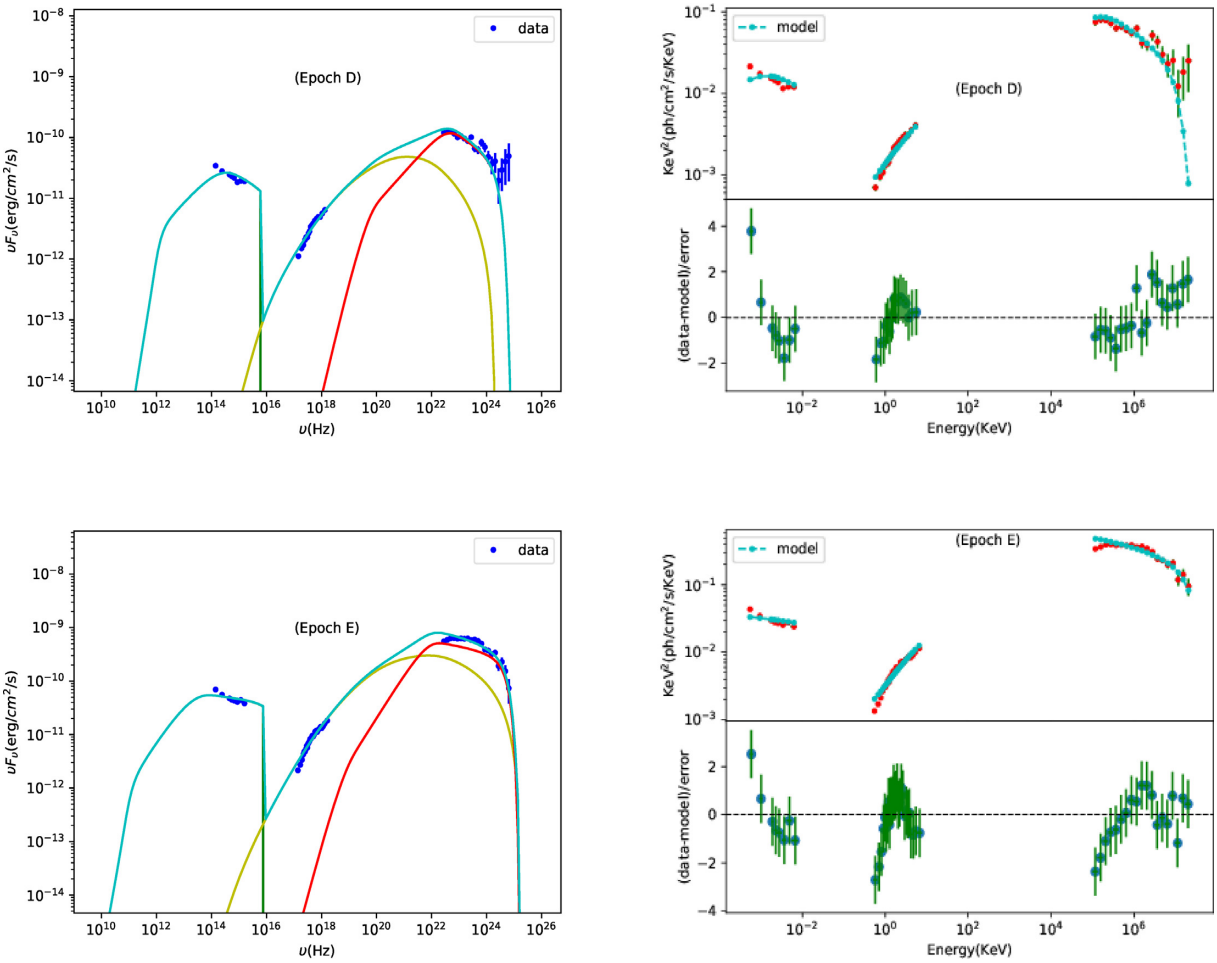

Figure 13. Model fits to the broad-band SED during epochs D and E. The panels have the same meanings as those of Fig. 12.

5 SUMMARY

We present our analysis of the multiband light curves of the FSRQ 3C 454.3 that includes γ-rays, X-rays, UV, optical, and IR spanning about 9 yr from 2008 August to 2017 February. The results are summarized below.

(i) Between the period 2008 August and 2017 February, 3C 454.3 showed large-amplitude optical/IR flares during four epochs identified in this work as A, B, D, and E. During epoch A, the optical flare has a counterpart in the γ-ray region. Cross-correlation analysis indicated that the optical and γ-ray flux variations are closely correlated with a lag of $2.5^{+1.5}_{-1.4}$ d with the optical lagging the γ-ray emission, pointing to difference in their emission regions. During epoch B, too, the optical flare has a corresponding γ-ray flare. From cross-correlation analysis we found that the flux variations in both the optical and gamma band are correlated with almost zero lag, pointing to co-spatiality of both the emission regions. During epochs D and E, though the optical flare has a similar magnitude to that of the flare at epochs A and B, the source is weak in the γ-ray band. Our analysis thus points to the detection of an optical flare with no γ-ray counterpart in 3C 454.3. The only other sources where such behaviour was observed are PKS 0208−512 (Chatterjee et al. 2013a), S4 1849+67 (Cohen et al. 2014), and 3C 279 (Pati no-Álvarez et al. 2018).

(ii) Broad-band SED modelling using a one-zone leptonic emission model was carried out on the four flaring epochs A, B, D, and E along with a quiescent epoch C for comparison. Relative to the quiescent state C, during the active state A and B, there is enhancement of the bulk Lorentz factor, which could explain the correlated optical and γ-ray flux variations. The observations of an optical flare with a weak/no γ-ray counterpart during epochs D and E could be due to a combination of parameters such as the bulk Lorentz factor, magnetic field, and electron energy density or changes in the location of the γ-ray-emitting region.

(iii) The available polarization observations during the period analysed here showed complex correlation to the optical flux changes. During a short-term optical flare (apart from the main flare) during epoch B, the degree of optical polarization was found to be correlated to the optical flux changes. However, during the flare at epoch E, the degree of optical polarization is anticorrelated to the optical *V*-band brightness during both the rising and falling part of the flare.

(iv) The source showed a complex colour ($V - J$)–magnitude (V) variability. During the epochs A and B, when optical and γ-ray variations are correlated, the source showed an RWB behaviour. For epoch D, the source showed an RWB trend for *V*-band brightness fainter than 15 mag, while for *V*-band magnitude brighter than 15 mag, it showed a BWB behaviour. For epoch E, when there

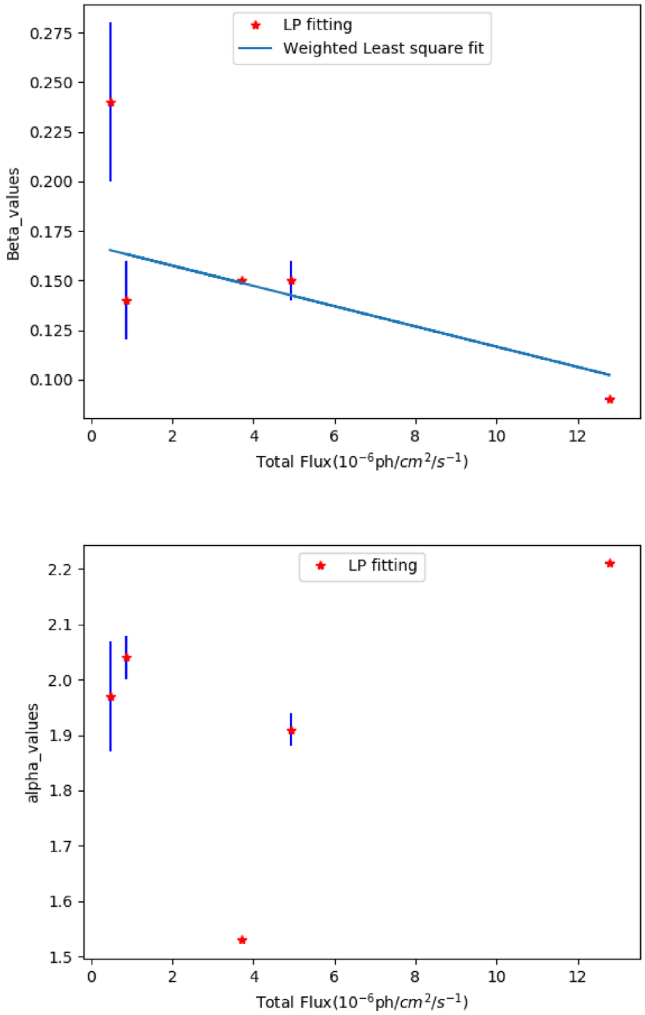

Figure 14. Variations of the parameters α and β with flux.

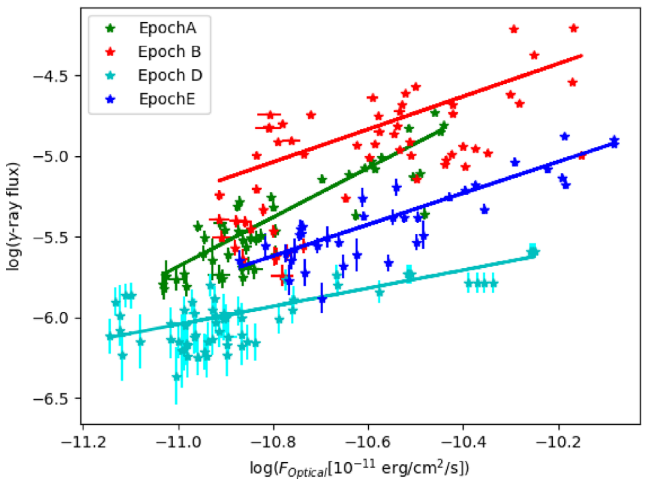

Figure 15. Optical flux versus γ-ray flux for epochs A,B,D, and E.

Table 4. Results of the linear least-squares fit to the optical and γ-ray flux measurements, during epochs A, B, D, and E.

Epoch	Slope	Intercept	Correlation coefficient
A	1.528 ± 0.112	11.128 ± 1.190	0.880
B	1.017 ± 0.144	5.945 ± 1.506	0.680
D	0.561 ± 0.048	0.132 ± 0.510	0.742
E	0.974 ± 0.068	4.901 ± 0.706	0.860

was an optical flare with no γ-ray counterpart, the source showed a BWB trend.

(v) The γ-ray spectra during all the five epochs were well described by an LP model. The curvature parameter β , which provides an indication of the cut-off present in the spectrum, is found to be lowest at the highest flux level and highest at the lowest flux level among the five epochs analysed here.

ACKNOWLEDGEMENTS

We thank the anonymous referee for his/her critical comments that helped to improve the manuscript. This research has made use of data, software, and web tools of the High Energy Astrophysics Science Archive Research Center (HEASARC), maintained by NASA's Goddard Space Flight Center. SMARTS observations of LAT-monitored blazars are supported by Yale University and Fermi GI grant NNX 12AP15G. JCI has received support from the NASA-Harriet Jenkins Pre-doctoral Fellowship Program, the NSF Graduate Research Fellowship Program (DGE-0644492), and the National Research Council's Ford Foundation Dissertation Fellowship. CDB, MMB, and the SMARTS 1.3 m and 1.5 m observing queue also receive support from NSF grant AST-0707627. We are grateful for photometry and polarimetry from Paul Smith's monitoring program at the Steward Observatory, which is supported by Fermi Guest Investigator grants NNX08AW56G, NNX09AU10G, and NNX12AO93G.

REFERENCES

Abdo A. A. et al., 2010a, ApJ, 710, 1271
Abdo A. A. et al., 2010b, ApJ, 716, 30
Abdo A. A. et al., 2011, ApJ, 733, L26
Acero F. et al., 2015, ApJS, 218, 23
Ackermann M. et al., 2010, ApJ, 721, 1383
Ackermann M. et al., 2015, ApJ, 810, 14
Antonucci R., 1993, ARA&A, 31, 473
Arnaud K. A., 1996, in Jacoby G. H., Barnes J., eds, ASP Conf. Ser. Vol. 101, Astronomical Data Analysis Software and Systems V. Astron. Soc. Pac., San Francisco, p. 17
Atwood W. B. et al., 2009, ApJ, 697, 1071
Begelman M. C. et al., 1987, ApJ, 322, 650
Błaerrorzdotejowski M., Sikora M., Moderski R., Madejski G. M., 2000, ApJ, 545, 107
Boettcher M., Mause H., Schlickeiser R., 1997, A&A, 324, 395
Bonning E. et al., 2012, ApJ, 756, 13
Bonning E. W. et al., 2009, ApJ, 697, L81
Böttcher M., 2007, Ap&SS, 309, 95
Böttcher M., Reimer A., Sweeney K., Prakash A., 2013, ApJ, 768, 54
Breeveld A. A., Landsman W., Holland S. T., Roming P., Kuin N. P. M., Page M. J., 2011, in McEnery J. E., Racusin J. L., Gehrels N., eds, AIP Conf. Ser. Vol. 1358, Gamma Ray Bursts 2010. Am. Inst. Phys., New York, p. 373

Burrows D. N. et al., 2005, Space Sci. Rev., 120, 165
Carnerero M. I. et al., 2015, MNRAS, 450, 2677
Chatterjee R. et al., 2012, ApJ, 749, 191
Chatterjee R. et al., 2013a, ApJ, 763, L11
Chatterjee R., Nalewajko K., Myers A. D., 2013b, ApJ, 771, L25
Cohen D. P., Romani R. W., Filippenko A. V., Cenko S. B., Lott B., Zheng W., Li W., 2014, ApJ, 797, 137
Coogan R. T., Brown A. M., Chadwick P. M., 2016, MNRAS, 458, 354
Dermer C. D., Schlickeiser R., 1993, ApJ, 416, 458
Dermer C. D., Yan D., Zhang L., Finke J. D., Lott B., 2015, ApJ, 809, 174
Diltz C., Böttcher M., 2016, ApJ, 826, 54
Dutka M. S. et al., 2013, ApJ, 779, 174
Edelson R. A., Krolik J. H., 1988, ApJ, 333, 646
Fossati G., Maraschi L., Celotti A., Comastri A., Ghisellini G., 1998, MNRAS, 299, 433
Gaskell C. M., Peterson B. M., 1987, ApJS, 65, 1
Gaskell C. M., Sparke L. S., 1986, ApJ, 305, 175
Gaur H., Gupta A. C., Wiita P. J., 2012, AJ, 143, 23
Gaur H., Gupta A. C., Wiita P. J., Uemura M., Itoh R., Sasada M., 2014, ApJ, 781, L4
Gehrels N. et al., 2004, ApJ, 611, 1005
Ghisellini G., Madau P., 1996, MNRAS, 280, 67
Ghisellini G., Maraschi L., 1989, ApJ, 340, 181
Ghisellini G., Tavecchio F., 2008, MNRAS, 387, 1669
Gu M. F., Lee C.-U., Pak S., Yim H. S., Fletcher A. B., 2006, A&A, 450, 39
Gupta A. C. et al., 2017, MNRAS, 472, 788
Hartman R. C. et al., 1993, ApJ, 407, L41
Hartman R. C. et al., 1999, ApJS, 123, 79
Isler J. C. et al., 2013, ApJ, 779, 100
Jorstad S. G. et al., 2012, preprint(arXiv:1205.0520)
Kalberla P. M. W., Burton W. B., Hartmann D., Arnal E. M., Bajaja E., Morras R., Pöppel W. G. L., 2005, A&A, 440, 775
Konigl A., 1981, ApJ, 243, 700
Kushwaha P., Gupta A. C., Misra R., Singh K. P., 2017, MNRAS, 464, 2046
Liao N. H., Bai J. M., Liu H. T., Weng S. S., Chen L., Li F., 2014, ApJ, 783, 83
MacDonald N. R., Marscher A. P., Jorstad S. G., Joshi M., 2015, ApJ, 804, 111
Mannheim K., 1993, A&A, 269, 67
Mao P., Urry C. M., Massaro F., Paggi A., Cauteruccio J., Künzel S. R., 2016, ApJS, 224, 26
Marscher A. P., Gear W. K., 1985, ApJ, 298, 114
Mattox J. R. et al., 1996, ApJ, 461, 396
Mücke A., Protheroe R. J., 2001, Astropart. Phys., 15, 121
Mücke A., Protheroe R. J., Engel R., Rachen J. P., Stanev T., 2003, Astropart. Phys., 18, 593
Nolan P. L. et al., 2012, ApJS, 199, 31
Paliya V. S., Stalin C. S., Ravikumar C. D., 2015a, AJ, 149, 41
Paliya V. S., Sahayanathan S., Stalin C. S., 2015b, ApJ, 803, 15
Paliya V. S., Diltz C., Böttcher M., Stalin C. S., Buckley D., 2016, ApJ, 817, 61
Pati no-Álvarez V. M. et al., 2018, MNRAS, 479, 2037
Peterson B. M. et al., 2004, ApJ, 613, 682
Raiteri C. M. et al., 2011, A&A, 534, A87
Sahayanathan S., Godambe S., 2012, MNRAS, 419, 1660
Sahayanathan S., Sinha A., Misra R., 2018, Res. Astron. Astrophys., 18, 035
Shah Z., Sahayanathan S., Mankuzhiyil N., Kushwaha P., Misra R., Iqbal N., 2017, MNRAS, 470, 3283
Sikora M., Begelman M. C., Rees M. J., 1994, ApJ, 421, 153
Smith P. S., Montiel E., Rightley S., Turner J., Schmidt G. D., Jannuzi B. T., 2009, preprint(arXiv:0912.3621)
Urry C. M., Padovani P., 1995, PASP, 107, 803
Vercellone S. et al., 2009, ApJ, 690, 1018
Vercellone S. et al., 2010, ApJ, 712, 405
Vercellone S. et al., 2011, ApJ, 736, L38
Vittorini V., Tavani M., Cavaliere A., Striani E., Vercellone S., 2014, ApJ, 793, 98
Vovk I., Neronov A., 2016, A&A, 586, A150
Wagner S. J., Witzel A., 1995, ARA&A, 33, 163

This paper has been typeset from a TEX/LATEX file prepared by the author.